Performance consideration of three-dimensional optoelectronic interconnection for intra-multichip-module clock signal distribution

Chunhe Zhao and Ray T. Chen

The structure, fabrication, and theory of a three-dimensional planarized optoelectronic clock signal distribution device, based on a thin light-guiding substrate in conjunction with a two-dimensional polymer holographic grating array, are described. We have demonstrated previously a 25-GHz 1-to-42 (6×7) highly parallel fan-out interconnect with a signal-to-noise ratio of 10 dB. We present theoretical research that focuses on generating a globally uniform fan-out distribution. An objective function aimed at equalizing the intensities among the fan-out beams is established. For an arbitrary $M \times N$ fan-out distribution, there are $M + N + 1$ sets of holograms needed to be recorded independently to provide the required equal fan-outs. The efficiency of each hologram is determined precisely. The angular misalignment, wavelength dispersion, and spot-size problems are discussed further, together with their tolerance requirements on the size of the photoreceivers integrated on the multichip modules. Employment of 0.25-pitch gradient index (GRIN) lenses as a collimator and as a focusing element is demonstrated experimentally. Optical beam profile manipulation and packaging tolerance are enhanced greatly with GRIN lenses. Finally, clock skew problems associated with the proposed system are discussed, and schemes to minimize the skew are proposed.

1. Introduction

The evolution of the integrated circuit technology from very large-scale integrated systems to ultra-large-scale integrated systems has led to increases in both the system size and the operation speed. As a result, system clock skew and data transfer rate become major concerns in the implementation of high-speed systems.[1] Multichip modules (MCM) are employed to provide higher clock speeds and circuit densities through minimizing the chip-to-chip interconnection distance. It is still difficult, however, to electrically distribute synchronous clock signals to the gigahertz region in intra-MCM and inter-MCM levels due to the required large fan-out, the associated skin effect, and the long interconnection path.

Optical interconnections, on the other hand, outperform electrical interconnections in the above-mentioned scenarios due to their performance advantages of speed and frequency-independent loss features.[2,3] Various applications using optics for communications in very large-scale integrated systems have been made, among which is the distribution of clock signals in a multiprocessor system that we discuss in this paper. Clock signals are used to synchronize the operations of various parts of the processor, hence clock skew is one of the measures of the performance of the system. Different schemes for providing optical clock signal distribution have been suggested based on fiber optics,[4–6] integrated waveguide optics,[7] and free-space optics.[8–10] For machine-to-machine interconnects, the fiber optics approach is usually adopted due to its flexibility and advantages in transmitting high-speed signals over large distances. However, on a chip-to-chip level, this approach is not suitable because of its bulkiness and associated packaging problems resulting from its point-to-point connection feature. Instead, the integrated waveguide interconnection approach is more adequate on this level. The free-space clock signal distribution, compared with the waveguide approach, allows higher connection density, a larger degree of freedom for the direction of interconnects, and often lower propagation delays. One of the major problems in applying the free-space

The authors are with the Microelectronics Research Center, Department of Electrical and Computer Engineering, University of Texas, Austin, Texas 78712.

Received 15 August 1996.
0003-6935/97/122537-08$10.00/0

approach in a real system lies in its difficulties in realizing a reliable packaging when massive fan-in and fan-out interconnects are required.

Recently we reported on a unique three-dimensional (3-D) free-space compact optical parallel fan-out interconnect for massive clock signal distribution, which, when integrated with vertical cavity surface-emitting lasers (VCSELs) and photoreceivers, can be used for intra-MCM and inter-MCM interconnects.[1] In Ref. 1 it was reported that as much as 25 harmonics can be transmitted with a system clock speed of 1 Gbit/s. This feature significantly reduces the clock jittering problem. Because of the 3-D interconnection feature of the reported device, it minimizes the employment of the real estate of semiconductor wafer surface, which is pivotal for a miniaturized, massive fan-out interconnect system with planar integration technology. More important, the parallel feature of the fan-out beams and the planarized compact device structure convert the unsolved 3-D spatial and angular multiple alignment problem into a single 2-D planar step, which greatly eases the packaging difficulties. For a high-speed electrical clock signal distribution, an H-tree fan-out structure has been employed frequently. Such a structure provides an equivalent delay and minimizes the reflection losses that are due to fan-out-induced impedance mismatch. It is impractical, however, from the optical interconnects point of view, to employ an equivalent optical H-tree structure with cascaded substrate-mode holograms as suggested by Yeh *et al.*[10] There is no intrinsic index mismatch (optical equivalence of impedance mismatch) problem affiliated with the 1-to-many fan-outs. Consequently, we can provide a large number fan-outs using a single substrate-mode hologram.[11] Furthermore, the implementation of a cascaded H-tree substrate-mode hologram array significantly increases the system insertion loss. For example, to provide 1-to-16 fan-out with the structure suggested in Ref. 10, the input clock signal has to interact with eight discrete holograms. With each hologram having an average of 75% diffraction efficiency, each output clock detector receives only 0.6% of the input power, which puts the system power budget in jeopardy. In this paper, we explore a different mesh structure of implementing the clock signal distribution system to reduce significantly the system insertion loss that is due to massive fan-outs. The fluctuations among all the output channels are minimized for the demonstrated 6×7 case[1] to obtain an equalized fan-out distribution. Limitations on the power and the allowable power ranges of the clock lasers that are due to the dynamic range of the available photodetectors are discussed further. The system requirement on the design of the clock lasers, especially their wavelength stability, are also discussed. The system alignment and spot size from the clock distribution device, which impose limits on the active area of the photodetector, are studied. System design aimed at reducing the size of the spot is analyzed further. Finally, clock skews of the system are discussed and schemes to minimize the skew are proposed.

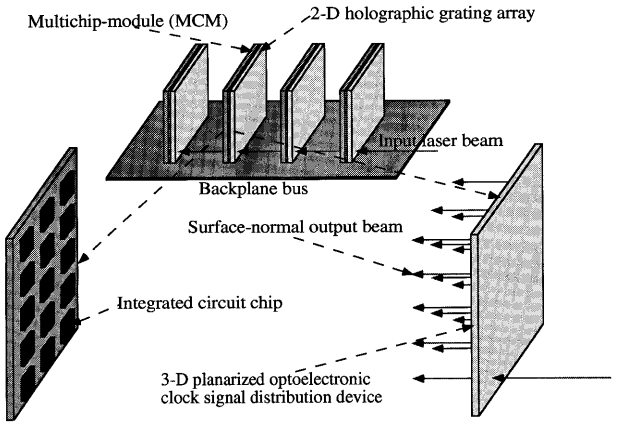

Fig. 1. Three-dimensional planarized optoelectronic clock signal distribution device in a multichip-module (MCM) system.

2. Optical Clock Signal Distribution System

Figure 1 shows how the 3-D planarized optoelectronic clock signal distribution device can be applied in a MCM system. The input clock signal is generated from a VCSEL. The optical clock signal is split and distributed by the clock signal distribution device. On the integrated circuit chip, the output clock signal is detected with an avalanche photodiode (APD) photodetector. In the previous experiment, a thin glass plate was used as the light-guiding medium. Fabrication of this device requires the formation of a photopolymer layer[11] on the surface of the wave-guiding plate. Arrays of holographic gratings are recorded afterward.[12] The structure of the clock signal distribution device[1] employs a thin light-guiding plate integrated with a 2-D holographic grating array on its surface. The configuration of the optical clock signal distribution device is described in Section 3. One of the most pivotal issues to make this device useful for a high-performance system is to provide the 1-to-many (many = 42 in Ref. 1) fan-outs with equal power. The power fluctuation among the 42 fan-out beams in Ref. 1 is as high as 25 dB, which makes the subsequent optical-to-electrical conversion impractical when considering the preset logic levels associated with it.

3. Power Budget Consideration: Minimization of Output Fluctuation

A. Clock Signal Propagation Analysis

Figure 2 shows a portion of the configuration of the clock signal distribution device containing a section of the microstructure of the holographic grating arrays attached to the wave-guiding plate.[1] The optical signal propagation inside the device is also shown. In this figure, the $\mathbf{K}_{ij}^{v}$'s ($v = x$ or y; $i = 1, \ldots, 6$; $j = 1$ for $v = x$ and $j = 1, \ldots, 7$ for $v = y$) are the grating vectors recorded in the photopolymer, the $\mathbf{k}$ and $\mathbf{k}'$s are the incident and diffracted wave vectors, and the

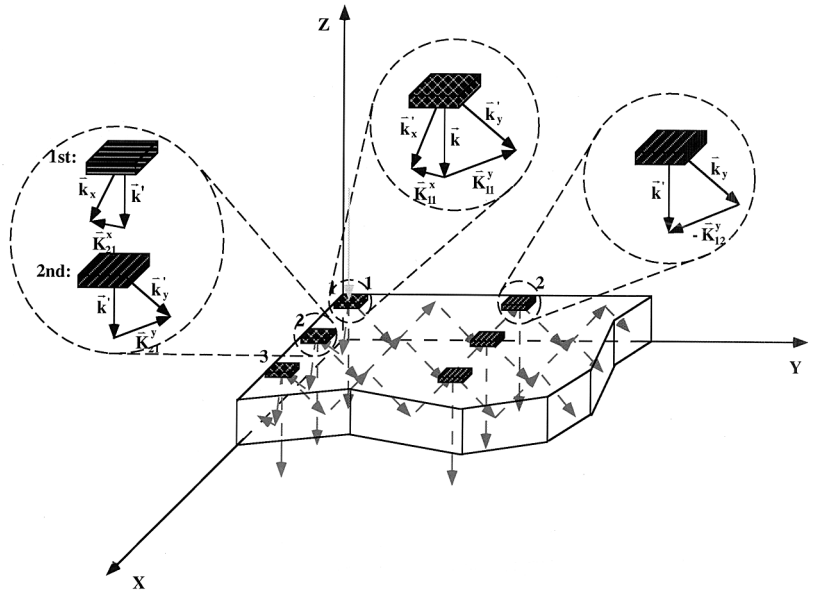

Fig. 2. Device configuration for free-space optoelectronic interconnection. The enlarged portions show the phase-matching conditions at three typical holographic grating sites.

subscript or superscript x's (y's) represent light beams or grating vectors along the x (y) direction. For Bragg diffraction, we have

$$\mathbf{k}' = \mathbf{k} - \mathbf{K}. \tag{1}$$

The phase-matching condition for the three representative planarized gratings of the device are shown clearly in Fig. 2, where we labeled the locations of the planarized gratings using two subscripts. The first is the position in the x direction and the second in the y direction. The sites with denotation $(i,1)$ ($i = 1, \ldots, M$, where M is the number of rows of planarized grating sites on the device) have two multiplexed holograms with grating vectors $\mathbf{K}_{i1}{}^{x}$ and $\mathbf{K}_{i1}{}^{y}$, respectively, whereas the subscript (i,j) ($i = 1, \ldots, M$; $j = 2, \ldots, N$, and N is the number of columns) represents location with only one planarized grating vector $\mathbf{K}_{ij}{}^{y}$. The first planarized multiplexed grating (1,1) is designed as an input coupler that couples the surface-normal input laser beam $\mathbf{k}$ into two substrate guided beams $\mathbf{k}_x{}'$ and $\mathbf{k}_y{}'$, with bouncing angles θ_x and θ_y greater than the total internal reflection angle, and propagating along the x and y directions, respectively.

Once it propagates to the subsequent planarized grating at site (1,2), the input substrate-guided beam $\mathbf{k}_y$ is partially coupled surface normally out of the device into $\mathbf{k}'$ by the grating $\mathbf{K}_{12}{}^{y}$. At location (2,1), the input substrate-guided beam $\mathbf{k}_x$ is first partially coupled into a surface-normal light beam $\mathbf{k}'$ by the grating $\mathbf{K}_{21}{}^{x}$, and then $\mathbf{k}'$ is cross coupled[13] partially into $\mathbf{k}_y{}'$ by grating $\mathbf{K}_{21}{}^{y}$, and then propagates along the y direction. Similar consideration is applicable to the remaining holographic grating sites. Each time, the coupling efficiency is not designed at 100%. It is clear from the above analysis that a 3-D free-space surface-normal parallel fan-out interconnect is constructed by the 2-D planarized grating arrays.

B. Minimization of Output Fluctuation

The system power budget for such a high-speed fan-out device is limited by the channels with the strongest and weakest fan-out intensities. Power uniformity is therefore crucial in the system design involving massive cascaded fan-outs. From the system implementation point of view, a uniform fan-out distribution can ease the design and fabrication of the very large-scale integrated circuit. For the optical clock signal distribution described herein, the minimum power of input optical signal is always limited by the output channel with the lowest fan-out intensity among the $M \times N$ fan-out beams. To optimize the performance of our device, aimed at providing a uniform fan-out intensity distribution, we define a transmission function as the power of the substrate-guided light beam transmitted from one hologram to the next. To simplify our calculation, we assume a unit input power. The transmission functions associated with the first column of multiplexed holographic gratings shown in Fig. 2 can then be represented by

$$T_2{}^{x} = \eta_1{}^{x},$$

$$T_i{}^{x} = T_{i-1}{}^{x}(1 - \eta_{i-1}{}^{x})(i = 3, \ldots, M), \tag{2}$$

where $T_i{}^{x}$ ($i = 2, \ldots, M$) is the power of light beam transmitted onto grating $(i,1)$ from grating $(i - 1,1)$ along the x direction, and $\eta_{i-1}{}^{x}$ ($i = 1, \ldots, M$) is the diffraction efficiency of the planarized gratings that couple the light beam out of or into the device along direction x. The multiplexed planarized gratings in column 1 couple the light beams propagating in direction x onto the second column, so the transmission

functions can be written as

$$T_{12}^{\,y} = \eta_{11}^{\,y},$$
$$T_{i2}^{\,y} = T_i^{\,x}\eta_i^{\,x}\eta_{i1}^{\,y}\ (i = 2, \ldots, M). \tag{3}$$

Similar to the above, here $T_{i2}^{\,y}$ $(i = 1, \ldots, M)$ means the intensity of the light beam transmitted to location $(i,2)$, and $\eta_{i1}^{\,y}$ $(i = 1, \ldots, M)$ is the diffraction efficiency of the grating at location $(i,1)$. Finally, for the rest of the planarized gratings, the transmission functions can be written easily as

$$T_{ij}^{\,y} = T_{i,j-1}^{\,y}(1 - \eta_{i,j-1}^{\,y})(i = 1, \ldots, M; j = 3, \ldots, N). \tag{4}$$

After we derive the transmission functions, the expressions for the fan-out intensities P_{ij}'s $(i = 1, \ldots, M; j = 1, \ldots, N)$ can be obtained by tracing the flow of optical energy from the input coupler (1,1) to the desired location (i,j), which are

$$P_{11} = 1 - \eta_1^{\,x} - \eta_{11}^{\,y},$$
$$P_{i1} = T_i^{\,x}\eta_i^{\,x}(1 - \eta_{i1}^{\,y})(i = 2, \ldots, M),$$
$$P_{ij} = T_{ij}^{\,y}\eta_{ij}^{\,y}\ (i = 1, \ldots, M; j - 2, \ldots, N). \tag{5}$$

Optimization of the performance of our device is to find an optimized distribution of diffraction efficiencies that will lead to a fan-out intensity distribution with a minimum power fluctuation and therefore an optimized power budget. For this purpose, an objective function[14] relating all terms of power fluctuations is generated. By optimizing the objective function, we can reach a uniform fan-out intensity distribution. For our problem, an obvious objective function is the sum of the square values of the differences between the fan-out intensities and their average.[14] Based on the above assumption, for our device with $M \times N$ fan-out beams, the average intensity is

$$\bar{P} = \frac{1}{M \times N}. \tag{6}$$

The objective function is then expressed as

$$E = E_1 + E_2, \tag{7}$$

where

$$\begin{cases} E_1 = \sum_{i=1}^{M}\sum_{j=1}^{N}\left(\frac{P_{ij}}{\bar{P}} - 1\right)^2 \text{ for } P_{ij} \geq \bar{P}\ (i = 1, \ldots, M; j = 1, \ldots, N), \\ E_2 = \sum_{i=1}^{M}\sum_{j=1}^{N}\left(\frac{\bar{P}}{P_{ij}} - 1\right)^2 \text{ for } P_{ij} < \bar{P}\ (i = 1, \ldots, M; j = 1, \ldots, N). \end{cases} \tag{8}$$

To minimize the power consumption of our device, we must have

$$\eta_M^{\,x} = 1,\ \eta_{iN}^{\,y} = 1\ (i = 1, \ldots, M), \tag{9}$$

for the outermost linear arrays where all energy is coupled out surface normally. To this point, the total number of unknown η's is $(M - 1) + (M \times N - M) = M \times N - 1$. We carried out the optimization process by minimizing the objective function E with respect to these $M \times N - 1$ η's. Note that the results derived through this calculation can be applicable to any integer combination of M and N. In accordance with our previous work,[1] we provide the result for $M = 6$ and $N = 7$. In Table 1 we summarize the optimized diffraction efficiency distribution for an equalized fan-out intensity of 0.0238 (1/42) per channel [Eq. (6)]. This result is further illustrated in Fig. 3, where the black bars are for $\eta_i^{\,x}$'s $(i = 1, \ldots, M)$ and the other bars are for $\eta_{ij}^{\,y}$'s $(i = 1, \ldots, M; j = 1, \ldots, N)$. The two-section structure at $y = 1$ and $x = 1, \ldots, 6$ clearly shows the diffraction efficiencies of a linear array of multiplexed holographic gratings. The diffraction efficiency of the polymer holographic gratings can be accurately controlled experimentally,[12] and diffraction efficiencies as high as 100% can be reached.[15] It is clear from Table 1 and Fig. 3 that, for arbitrary $M \times N$ fan-outs, there are $M + N + 1$ sets of holograms with different diffraction efficiencies along the x and y directions, respectively. For the specific case demonstrated,[1] $M = 6$ and $N = 7$, we need 14 sets of holograms to provide the required equal fan-outs. Table 1 also indicates that, for an arbitrary matrix of $M \times N$, beginning from the second

Table 1. Optimized Diffraction Efficiency for Uniform Fan-Out Distribution for the Case $M = 6$, $N = 7$.

$\downarrow x$ / $\eta_{ij}^{\,y}$ / $\rightarrow$ / y	1		2	3	4	5	6	7
	$\eta_i^{\,x}$ Ⓧ	$\eta_{i1}^{\,y}$ ⊖	Ⓨ	Ⓨ	Ⓨ	Ⓨ	Ⓨ	Ⓨ
1	0.833	0.143	0.167	0.200	0.250	0.333	0.500	1.000
2	0.200	0.857	0.167	0.200	0.250	0.333	0.500	1.000
3	0.250	0.857	0.167	0.200	0.250	0.333	0.500	1.000
4	0.333	0.857	0.167	0.200	0.250	0.333	0.500	1.000
5	0.500	0.857	0.167	0.200	0.250	0.333	0.500	1.000
6	1.000	0.857	0.167	0.200	0.250	0.333	0.500	1.000

Note: The symbol Ⓧ means that the holographic gratings in that column couple the light beam propagating along the x-direction surface normally out of the substrate, Ⓨ means that gratings in that column couple the light along the y-direction surface normally out of the substrate, and ⊖ means that the gratings in that column couple the light into the y direction.

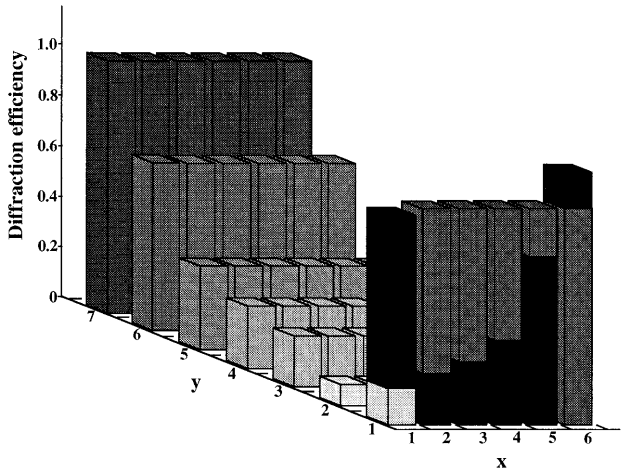

Fig. 3. Optimized diffraction efficiency distribution for uniform fan-out for the case $M = 6$ and $N = 7$. The solid black bars are for $\eta_i{}^x$'s ($i = 1, \ldots, M$) and the other bars are for $\eta_{ij}{}^y$'s ($i = 1, \ldots, M$; $j = 1, \ldots, N$).

row, the values of $\eta_i{}^x$'s ($i = 2, \ldots, M$) varies as

$$\eta_i{}^x = \frac{1}{M + 1 - x} \, (i = x = 2, \ldots, M), \qquad (10)$$

where x is the location of the hologram along direction x. The same reciprocal relation is also valid for $\eta_{ij}{}^y$'s ($1 = 1, j = 1$, and $i = 1, \ldots, M; j = 2, \ldots, N$) along direction y, i.e.,

$$\eta_{ij}{}^y = \frac{1}{N + 1 - y} \, (i = 1; j = y = 1;$$

$$i = 1, \ldots, M; j = y = 2, \ldots, N). \qquad (11)$$

The above observation can be used experimentally in the recording of the holographic grating to greatly reduce the degree of complexity. By precisely controlling the diffraction efficiencies of the holographic grating arrays according to our optimized result, one can obtain a uniform fan-out intensity distribution.

For an optimized optical clock signal distribution device without significant reflection and propagation losses inside the substrate, the intensity per output channel with an input intensity P_{in} and a total of $M \times N$ channels can be written as

$$P_{\text{out}} = \frac{(1 - R) P_{\text{in}}}{M \times N}, \qquad (12)$$

where R is the reflectivity of the input grating coupler. Without any antireflection coating mechanism, experiments showed $R \approx 11\%$. For the detection of the optical clock signal, APD receivers are more suitable than p-i-n receivers for our system. This is because of their relatively better sensitivity and higher input power dynamic range. Higher dynamic range can be obtained with APD receivers. For short-wavelength (0.8–0.9-μm) detection, silicon APD receivers are used mostly, and a dynamic range of approximately 40–50 dB has been obtained. In the long-wavelength (1.1–1.6-μm) region, germanium and III-V alloys such as InGaAsP and GaAlAsSb give better performances, and a dynamic range of 25–40 dB has been reported.[16] The sensitivity of the receivers, that is, the minimum optical signal power required at the optical detector input for a desired receiver performance, determines the minimum power requirement of an optoelectronic system. For a bit error rate of 10^{-9}, operating at 500 Mbit/s and a multiplied primary dark current of 1000 nA, the sensitivity of silicon APD's at 0.85 μm is around −45 dBm; for germanium and InGaAs APD's, the sensitivities at 1.3 μm are approximately −41 and −42 dBm, respectively.[16] All the above sensitivities would result in a minimum signal power of around 0.04 μW at the input of the detectors. On consideration of the reflection from the input port, Eq. (12) gives a minimum input power onto the clock device of 1.89 μW, which can be achieved easily with state-of-the-art VCSEL technology.[17,18] With an average dynamic range of 30 dB, the input power range over which the receivers can perform properly without distortion and saturation lies between 1.89 μW and 1.89 mW.

4. Alignment Consideration of the Optical Clock Signal Distribution System

Several factors would affect the packaging of the optical clock signal distribution system when integrated with clock lasers and receivers. Among others, the most important ones that are discussed in this section are lateral and angular misalignment and wavelength instability and divergence of spot size.

A. Lateral and Angular Misalignments

Lateral misalignment means the misalignment of the device position, which is due to the inaccuracy in its x and y directions (Fig. 1). It can be divided into absolute and relative misalignments. With the current self-aligned, flip-flop solder bump bonding process,[19] the absolute lateral misalignment can be controlled with an accuracy of ~1 μm. Once coupled into the substrate, the signal beam travels toward the photodetector. A lateral misalignment in the clock laser results in an equivalued spatial shift of the output signal beam.

The influence of the angular misalignment on the lateral misalignment arises from the phase mismatch between the input signal beam and the grating vector when the incident angle deviates from the Bragg angle. Figure 4 shows the phase-matching condition of a hologram for surface-normal coupling. For Bragg diffraction, we have[20]

$$\begin{pmatrix} -\sin \gamma \\ \cos \gamma \end{pmatrix} = \begin{pmatrix} \dfrac{\sin \theta}{n} - \dfrac{K}{\beta} \sin \phi \\ \sqrt{1 - \dfrac{\sin^2 \theta}{n^2} - \dfrac{K}{\beta} \cos \phi} \end{pmatrix}, \qquad (13)$$

where n is the refraction index of the hologram, $\beta = 2\pi n/\lambda$ is the propagation constant of light with wave-

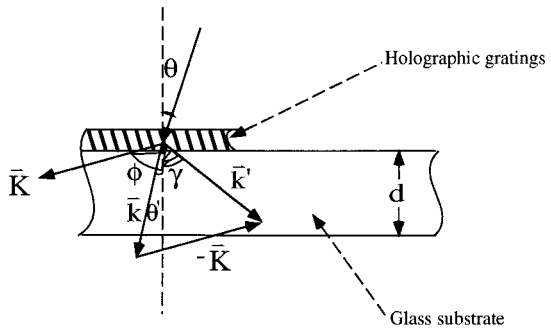

Fig. 4. Phase-matching diagram correlating the grating vector **K**, the incident beam **k**, and the diffracted beam **k′** for a 1-D array of slanted holographic gratings. d, substrate thickness.

length λ, and the meanings of γ, θ, and K are as shown in Fig. 4. After eliminating φ from Eq. (13) and differentiating the resulting equation, we obtain

$$\Delta\gamma = \frac{\left[\sin\theta - n\left(\frac{K^2}{2\beta^2} - 1\right)\sin\gamma\right]\cos\theta}{\left[\left(\frac{K^2}{2\beta^2} - 1\right)\sin\theta - n\sin\gamma\right]n\cos\gamma}\Delta\theta. \quad (14)$$

If the number of total internal reflection of the specific light beam shown in Fig. 4 is m, then the corresponding device length is

$$L = md\tan\gamma. \quad (15)$$

From Eqs. (14) and (15), a variation of the angle of the input light beam will lead to a spatial shift of the fan-out beam on the device surface of

$$\Delta L = \frac{[\tan(\gamma + \Delta\gamma) - \tan\gamma]}{\tan\gamma}L, \quad (16)$$

and Δγ is given by Eq. (15). This relation is shown schematically in Fig. 5. In our calculation, we assumed the wavelength of the VCSEL as λ = 850 nm, n = 1.512 (polymer waveguide), θ = 0° (surface normal), γ = 45°, and L is taken as the longest distance, that is $(2d\tan\gamma) \times [(6-1) + (7-1)] = 2.2$ cm. It

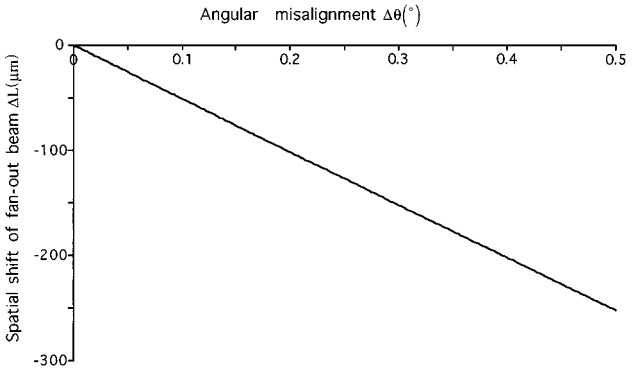

Fig. 5. Variation of the spatial position of the fan-out beam on the device surface with respect to the angular misalignment of the input signal beam.

can be seen from Fig. 5 that, within a small angular misalignment of the input light beam, ΔL changes linearly with Δθ, which can also be seen from Eqs. (14) and (16). However, Fig. 5 also shows that the control of the angular alignment should not be so easy a task. To keep the spatial shift of the output signal beam below an error range of ±50 μm (for a silicon APD, the typical size of an active area is of the order of ~100 μm at 1 GHz), the angular misalignment should be within ±0.1°. This stringent requirement is relaxed significantly by applying a gradient index (GRIN) lens, which is addressed in Subsection 4.B.

B. Wavelength Instability of the Clock Laser

Variation of lasing wavelength from the clock laser influences the spatial shift of the output signal beam by the same mechanism as does the angular misalignment. In fact this mechanism has been used in the design of a wavelength division demultiplexing device.[21] The theory behind this mechanism is that a deviation in wavelength of the input signal beam will lead to an angular deviation of the diffracted beam from the Bragg angle. This comes out as the spatial shift of the output beam.

In general, the emission line width from VCSEL's can be as narrow as less than 1 Å. The misalignment that is due to this spectral width factor can thus be determined to be 0.17 μm, which can be ignored when one considers that the normal size of the photodetector active area is of the order of ~100 μm. For a VCSEL with three-quantum well InGaAs/GaAs active region, the lasing wavelength varies with temperature in a rate[22] of ~0.5 Å/K. To maintain a spatial shift within ±50 μm, the allowable temperature variation is ±5.8 K, which is within the limit of the contemporary optoelectronic temperature stability control level.[23]

For the VCSEL's discussed above, the active light-emitting window has a diameter of 5 μm and a lasing divergence angle of 5°. After propagating 2.2 cm in the substrate, the spot size becomes 615 μm, which renders the detector impossible to respond in comparison with the ~100-μm size of the detector active region for an 1-Gbit/s system. To make the system practical, precise beam profile manipulation is required. Here we introduce GRIN lenses into our system. A 0.25-pitch GRIN lens is suitable for our application. The simple architecture of the clock distribution system with GRIN lenses is depicted in Fig. 6(a). After the signal beam from the VCSEL travels through the GRIN lens, it will become collimated. Theoretically, as long as the collimated beam keeps surface-normally incident onto the GRIN lens at the output end, it will be focused into a diffraction-limited spot. Figure 6(b) shows the output near-field beam pattern at the end facet of the 0.25-pitch output GRIN lens that functions as a focusing element. If the input signal beam has a misalignment Δθ in its input angle as shown in Fig. 7, then the ray matrix[24] gives the spot shift at the fo-

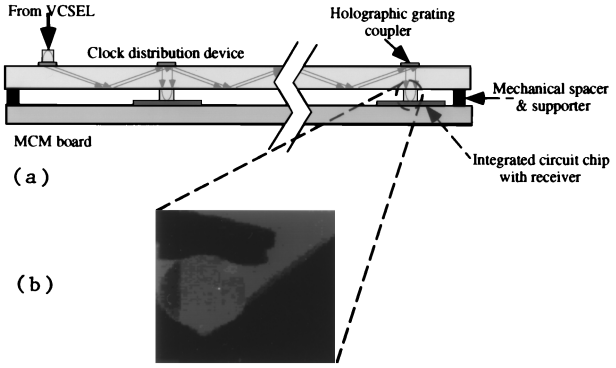

Fig. 6. (a) Side view of the proposed system architecture involving GRIN lenses as collimating and focusing elements. (b) Near-field profile of the focal spot shown at the output facet of the 0.25-pitch output GRIN lens with a spot size of 70 μm.

cusing end as

$$\Delta r = \frac{\Delta\theta}{N_0\sqrt{A}}, \tag{17}$$

where N_0 is the refractive index on the central axis of the GRIN lens and $\sqrt{A}$ is the index gradient constant. At $\lambda = 0.85$ μm, $N_0 = 1.6457$ and $\sqrt{A} = 0.423$. With a misaligned angle of 2°, the shift of the output spot from the central axis of the GRIN lens is $\Delta r \approx 50$ μm, whereas without the GRIN lens this same angular misalignment would give ~1 mm from Fig. 5. Thus the use of a GRIN lens in our clock signal distribution system greatly eases the angular tolerance. The current commercially available GRIN lenses have a minimum diameter of 1 mm. For the photodetectors to collect all the output energy and to tolerate the spatial shift induced by the misalignment of the input port, the diameter of the GRIN lenses at the output port should be larger than that at the input port. The spot size shown in Fig. 6(b) is 70 μm (3 dB), which is less than the diameter of the photodetector employed. The enlargement is due to the Gaussian beam effect.

5. Clock Skew Analysis

Clock skew is another important factor limiting the performance of the optical clock distribution system. It can be divided into deterministic and undeterministic[5] skew. Actually, the deterministic skew can be eliminated by properly adjusting the transmission line paths of the clock signal distribution.

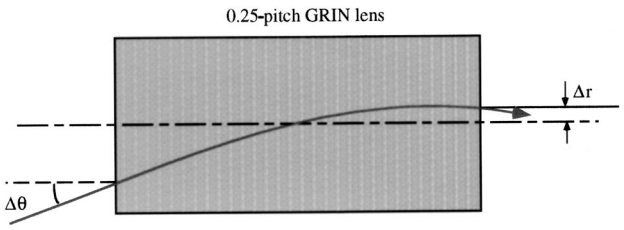

Fig. 7. Parameters in the ray-tracing solution of the 0.25-pitch GRIN lens with an incident angle deviation of Δθ.

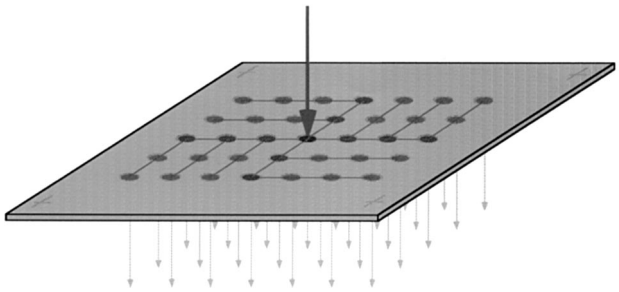

Fig. 8. Proposed structure to eliminate clock skew of the clock distribution device that is due to path differences.

The deterministic clock skew associated with the device we investigated here can be calculated by considering the longest path the clock signal travels inside the wave-guiding plate, which is the path between the input coupler at location (1,1) and the output coupler at (6,7) (see Table 1). If we assume a light beam bouncing angle of $\gamma = 45°$ and a substrate thickness of $d = 1$ mm as shown in Fig. 4, this longest light path would be

$$L = 2d \tan\gamma \times [(6-1) + (7-1)] = 2.2 \text{ cm}. \tag{18}$$

So the largest clock skew incurred by the planar clock distribution of the device is

$$t_{\text{skew}} = \frac{L}{c/n} = 110 \text{ ps}, \tag{19}$$

where $n = 1.5$ is the refractive index of the glass substrate. This corresponds to a speed of 9.1 GHz.

To eliminate the clock timing jitter, higher-order harmonics will be needed to maintain the edges of binary signals. The present system goes as high as the ninth harmonic with a system clock speed of 1.1 GHz. The above device-induced clock skew can be reduced further by employing the architecture as in Fig. 8. In Fig. 8 we input the light signal from the central pixel on which four multiplexed holograms are recorded to provide a 1-to-4 fan-out. With this scheme, the clock skew of the above-the-clock distribution device can be reduced by half of what we obtained above.

Undeterministic clock skew mainly comes from receivers. This can be subdivided into static and temporal skews.[25] The static skew is due to a finite response time of the receiver to a binary pulse edge. It is fixed for a given detector but varies for different receivers because of uncertainties that exist in fabrication processes and power supply. The temporal skew is due to the noise coming from the receiver itself or the jitter of clock laser. This noise will raise the overall level of the waveform, increase the threshold crossing time of the optical receiver, and therefore worsen the clock jittering problem.

6. Conclusions

In summary, we presented the theory of the intensity optimization of a massive fan-out optical clock signal distribution, based on a 1-mm light-guiding substrate

in conjunction with 2-D planarized holographic grating arrays. The theoretical result shows that a uniform fan-out intensity distribution exists. Such an optimized condition among $M \times N$ fan-outs can be attained by precisely controlling the diffraction efficiencies of the holographic gratings according to the optimized results. A reciprocal relationship of the diffraction efficiencies with their position along the x and y directions are observed, which, if applied in the process of recording the holographic gratings, would reduce greatly the degree of complexity. Power budget consideration is discussed based on the optimization results, and a minimum input power of 1.89 μW is found to ensure the normal operation of the system with 42 fan-outs. Packaging-related issues, such as the angular misalignment and wavelength toleration are considered. GRIN lens collimating and focusing mechanisms are introduced into the clock distribution system with the proven experiment result. It was found that not only can the GRIN lens function as the collimating and focusing elements for optical signals, but also as a packaging reliability enhancer that makes the angular misalignment tolerance an order of magnitude larger than that without the use of a GRIN lens.

This research was sponsored by Cray Research, State of Texas, and the Defense Advanced Research Project Agency Center of Optoelectronics, Science, and Technology.

References

1. S. Tang and R. T. Chen, "1-to-42 optoelectronic interconnection for intra-multichip-module clock signal distribution," Appl. Phys. Lett. **64,** 2931–2933 (1994).
2. J. W. Goodman, F. J. Leonberger, S.-Y. Kung, and R. A. Athale, "Optical interconnections for VLSI systems," Proc. IEEE **72,** 850–866 (1984).
3. M. R. Feldman, C. C. Guest, T. J. Drabik, and S. C. Esener, "A comparison between optical and electrical interconnects for fine grain processor arrays based on interconnect density capacities," Appl. Opt. **28,** 3820–3829 (1989).
4. A. J. Cooper, "Clock distribution using optical wavelength division multiplexing techniques," in *Fiber Optic Datacom and Computer Networks*, J. E. Hayes and J. Pazaris, eds., Proc. SPIE **991,** 27–31 (1988).
5. R. L. Khalil, L. R. McAdams, and J. W. Goodman, "Optical clock distribution for high speed computers," in *Fiber Optic Datacom and Computer Networks*, J. E. Hayes and J. Pazaris, eds., Proc. SPIE **991,** 32–41 (1988).
6. P. J. Delfyett, D. H. Hartman, and S. Z. Ahmad, "Optical clock distribution using a mode-locked semiconductor laser diode system," J. Lightwave Technol. **9,** 1646–1649 (1991).
7. S. Koh, H. W. Carter, and J. T. Boyd, "Synchronous global clock distribution on multichip modules using optical waveguide," Opt. Eng. **33,** 1587–1595 (1994).
8. B. D. Clymer and J. W. Goodman, "Optical clock distribution to Silicon chips," Opt. Eng. **25,** 1103–1108 (1986).
9. S. J. Walker and J. Jahns, "Optical clock distribution using integrated free-space optics," Opt. Commun. **90,** 359–371 (1992).
10. J. H. Yeh, R. K. Kostuk, and K. Y. Tu, "Board level H-tree optical clock distribution with substrate mode holograms," J. Lightwave Technol. **13,** 1566–1578 (1995).
11. W. J. Gambogi, A. M. Weber, and T. J. Trout, "Advances and applications of Dupont holographic photopolymer," in *Holographic Imaging and Materials*, T. H. Jeong, ed., Proc. SPIE **2043,** 2–13 (1993).
12. R. T. Chen, H. Lu, D. Robinson, M. Wang, G. Savant, and T. Jannson, "Guided-wave planar optical interconnects using highly multiplexed polymer waveguide holograms," J. Lightwave Technol. **10,** 888–897 (1992).
13. S. K. Case, "Coupled-wave theory of multiply exposed thick holographic gratings," J. Opt. Soc. Am. **65,** 724–729 (1975).
14. K. W. Cattermole and J. J. O'Reilly, *Optimization Methods in Electronics and Communication* (Wiley, New York, 1984).
15. L. H. Lin, "Hologram formation in hardened dichromated gelatin films," Appl. Opt. **8,** 963–966 (1969).
16. T. V. Muoi, "Optical design for high-speed optical-fiber systems," J. Lightwave Technol. **LT-2,** 243–267 (1983).
17. J. L. Jewell, J. P. Harbison, A. Scherer, Y. H. Lee, and L. T. Florez, "Vertical-cavity surface-emitting lasers: design, growth characterization," IEEE J. Quantum Electron. **27,** 1332–1346 (1991).
18. K. Uomi, S. J. B. Yoo, A. Scherer, R. Bhat, N. C. Andreadakis, C. E. Zah, M. A. Koza, and T. P. Lee, "Low threshold, room temperature pulsed operation of 1.5 μm vertical-cavity surface-emitting lasers with an optimized multi-quantum well active layer," IEEE Photon. Tech. Lett. **6,** 317–319 (1994).
19. M. J. Wale and C. Edge, "Self-aligned flip-chip assembly of photonic devices with electrical and optical connections," IEEE Trans. Components, Hybrids, Manuf. Technol. **13,** 780–786 (1990).
20. H. Kogelnik, "Coupled wave theory for thick hologram gratings," Bell Syst. Tech. J. **48,** 2909–2947 (1969).
21. M. M. Li and R. T. Chen, "Two-channel surface-normal wavelength division demultiplexer using substrate guided waves in conjunction with multiplexed waveguide holograms," Appl. Phys. Lett. **66** (3), 262–264 (1995).
22. H. Deng, C. C. Lin, D. L. Huffaker, Q. Deng, and D. G. Deppe, "Temperature dependence of the transverse lasing mode in vertical-cavity lasers," J. Appl. Phys. **77,** 2279–2286 (1995).
23. C. Lin, *Optoelectronic Technology and Lightwave Communications Systems* (Van Nostrand Reinhold, New York, 1989), Chap. 15.
24. SELFOC Product Guide, NSG American, Inc., Somerset, N.J.
25. R. L. Khalil, "Clock skew analysis for Si and GaAs receivers," in *Optical Interconnects in the Computer Environment*, J. Pazaris and G. R. Willenbring, eds., Proc. SPIE **1178,** 171–176 (1989).